Transformed Workspace Adaptive Mapping Based Master-Slave Operation Control for Hydraulic Manipulator

Shizhao Zhou [ID], Yangxiu Xia [ID], Manzhi Qi [ID], Deqing Mei [ID], and Zheng Chen [ID], *Senior Member, IEEE*

Abstract—The unstructured working environment poses a significant challenge in achieving autonomous operation of hydraulic manipulators, which has led to the widespread use of master-slave operation in practice. However, it is typical for the hydraulic manipulator and the master robot to exhibit different mechanical configurations (i.e., master-slave heterogeneity). This can result in excessive range differences and low similarity between the master and slave workspaces, leading to the hydraulic manipulator being unable to accurately reproduce the actual intentions of the operator. Furthermore, the nonlinear dynamics and end-load disturbance during operation significantly affect the control accuracy of the hydraulic manipulator. To address the aforementioned challenges in master-slave operation, this article proposes a novel control scheme based on transformed workspace adaptive mapping (TWAM). By reconstructing the transformed workspace, the similarity between the master and slave workspaces has been improved. Furthermore, the accurate utilization ratio (AUR) of the slave workspace has been expanded through an adaptive command mapping algorithm. Moreover, a model-based controller that takes into account nonlinear dynamics and the end-load disturbance is developed to ensure precise operation in various loaded states. Finally, a series of experiments are conducted, and the results have verified the practical applicability and effectiveness of the designed method.

Index Terms—End-load disturbance, heterogeneity mapping, hydraulic manipulator, master-slave operation, nonlinear control.

I. INTRODUCTION

IN recent years, the working occasions of hydraulic manipulators have gradually expanded from simple factory settings to the unstructured environment [1], which has made it significantly more challenging to realize autonomous operation. In comparison, the master-slave operation, where the operator sends commands from the master devices and implements closed-loop control on the slave device to complete tasks [2], is a more realistic and feasible approach for manipulators to operate in unstructured environments [3], [4]. However, the common application of hydraulic manipulators in unstructured environments, represented by underwater operations [5], [6], requires precise and efficient task completion. The performance of the master-slave operation of hydraulic manipulators at this stage is inadequate to meet the operational requirements, with the most crucial problems being the master-slave heterogeneity and low control accuracy.

The master-slave heterogeneity, characterized by an excessive range difference and low similarity between the master and slave workspaces, poses a significant challenge for master-slave operation [7]. Specifically, the tradition position-position mapping (PPM) method tends to be inefficient in fully utilizing the slave workspace without exceeding the boundary limits. This is because the excessive range difference requires the adoption of larger scaling factors to ensure the full utilization of the slave workspace [8]. However, since the workspace mapped by PPM is similar to the master workspace, the low similarity between the master and slave workspaces means that it is challenging to guarantee the mapped workspace does not exceed the slave boundaries [9]. Moreover, the low similarity between the mapped workspace and the master workspace further results in an inaccurate representation of the operator's intention, potentially leading to the execution of excessive or erroneous operations, thereby endangering the operation target [10]. Recently, a number of approaches have been proposed for addressing master-slave heterogeneity. Sun et al. [11], [12] introduced a workspace tuning approach to update the scaling gains and the barriers of workspace to the extent that the robot's workspace can adapt to different task spaces. Li et al. [13], [14] designed an incomplete orientation mapping method to cope with the heterogeneity caused by different degrees of freedom between the master and slave devices. Chen et al. [15], [16]

proposed a hybrid workspace mapping method to enhance the transparency performance of teleoperation. The aforementioned studies have both achieved good performance on traditional industrial robots. Nevertheless, the larger dimensions and the uncertain configuration of degree of freedom (DOF) of hydraulic manipulators result in a greater range difference and a lower similarity between master and slave workspaces. Consequently, further research is urgently required to develop more effective heterogeneous mapping methods for hydraulic manipulators based on the aforementioned research.

Besides, the efficiency of master-slave operations is also dependent on the control accuracy of hydraulic manipulators. Given that traditional control methods such as PID cannot achieve satisfactory accuracy due to the nonlinear dynamics of hydraulic manipulators [17], [18], various model-based controllers have been developed. Mattila et al. [19], [20] introduced virtual decomposition control (VDC) for heavy-duty hydraulic manipulators and demonstrated noteworthy control performance. Xu et al. [21], [22] designed a hierarchical decoupling controller and obtained satisfactory performance for hydraulic manipulators. Yao et al. [23], [24] proposed a continuous robust integral of the sign of the error control approach (RISE) to achieve asymptotic tracking under various disturbances. These aforementioned studies can provide valuable references for improving the control accuracy of hydraulic manipulators. However, another issue that should not be overlooked in practice is the end-load state of the robot during operation, which can cause additional dynamic disturbance, thereby further limiting the control accuracy of the manipulator. Recently, an increasing number of researchers have noted the influence of end-load on task completion. Sun et al. [25], [26] presented a dynamic and kinematic adaptation law to optimize the control performance of the Franka robot when picking unknown weights. Jin et al. [27] proposed an online payload identification algorithm based on a recursive formulation and achieved the estimation for payloads weighing between 20 and 75 kg on a quadruped robot. Ngo et al. [28] introduced an adaptive WNN control algorithm to approximate unknown dynamics and transport various types of objects. These studies have achieved positive results for specific robots in laboratory settings. Nevertheless, it still remains to be investigated how to improve the operation accuracy of hydraulic manipulators in unstructured environments by integrating their nonlinear dynamics and the end-load disturbance.

To address the aforementioned challenge, thereby achieving precise and efficient master-slave operation for hydraulic manipulators, this article proposes a novel master-slave operation control based on transformed workspace adaptive mapping (TWAM). Specifically, for the heterogeneous mapping, a novel transformed coordinate system is defined to ensure a higher similarity between the slave workspace and the mapped workspace. Additionally, an adaptive mapping approach is developed to ensure that the accurate master-slave operation can be achieved in a larger range of the slave workspace. In terms of the control accuracy, a direct/indirect adaptive robust controller (DIARC) is designed to ensure precise operation in various loaded states. Finally, experiments are conducted to demonstrate that the hydraulic manipulator controlled by the designed method can cope with the influence of master-slave heterogeneity and end-load disturbance, thereby executing the master-slave operation precisely and efficiently in unstructured environments such as underwater. The main contributions are as follows:

1) The TWAM method is proposed to address the restrictions imposed by master-slave heterogeneity on the operational performance of hydraulic manipulators. A transformed workspace is established to unify the dimensions of the master and slave workspaces as a basis for adaptive command mapping. In positioning mapping for precise operation, the variable-scale one-to-one-axis mapping (VOM) method is proposed for improving the similarity between the mapped workspace and the slave workspace, as well as improving the accurate utilization of the slave workspace. As a result, the positioning mapped command can accurately reproduce the operator's intent within the largest possible slave workspace, thereby guaranteeing the operational effectiveness. Furthermore, navigation mapping is employed to achieve complete traversal of the slave workspace, thus enabling the manipulator to more swiftly approach the operation target and enhancing operational efficiency.

2) A DIARC approach with end-load disturbances compensation is designed to guarantee the operational precision of hydraulic manipulator under varying end-load states. The ARC technique is adopted to cope with the higher-order nonlinear dynamics of hydraulic manipulators. More importantly, to address the impact of varying end-load states on the control performance, the dynamics effects of end-load are incorporated into the overall system dynamic model in the form of the unknown model parameter and integrated into the ARC feed-forward model compensated control law. And the load disturbance compensation is updated in real time by the parameter adaptation, thereby achieving precise control of hydraulic manipulators under varying end-load states.

3) A series of comparative experiments are conducted to verify the effectiveness of the designed TWAM approach and the proposed nonlinear controller. And the master-slave precise grasping of the hydraulic manipulator in water is realized based on the proposed master-slave operation control scheme.

The remaining parts of this article are arranged as follows. The designed TWAM method is presented in Section II. Section III gives the design procedures of the DIARC with end-load disturbance compensation. Experimental setup and results are presented in Section IV. Finally, Section V concludes this article.

II. TWAM-BASED MASTER-SLAVE OPERATION

The framework of the proposed TWAM-based hydraulic manipulator master-slave operation control is shown in Fig. 1. The TWAM, a novel heterogeneous mapping method, can effectively eliminate the influence of master-slave heterogeneity.
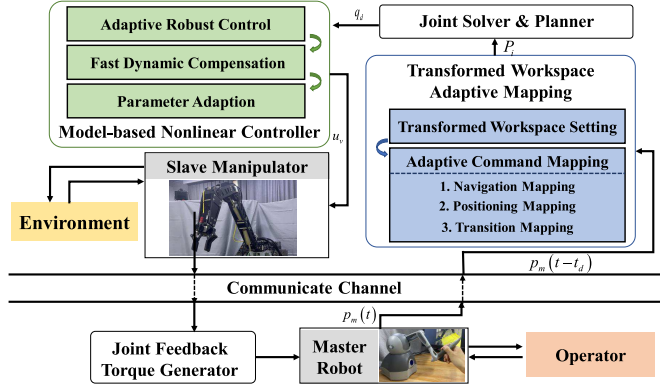
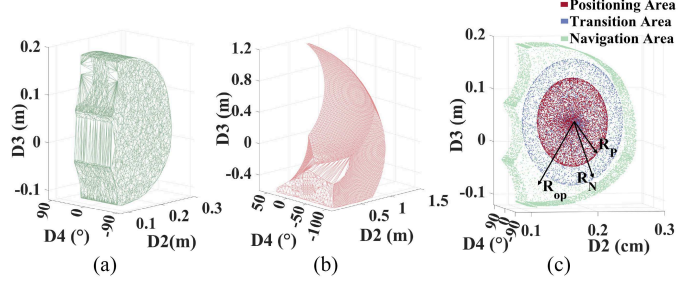Fig. 1. Framework of TWAM-based master-slave operation control.

Fig. 2. Last three-dimensions space of transformed workspace and adaptive workspace characterization. (a) The master last three-dimensional transformed workspace. (b) The slave last three-dimensional transformed workspace. (c) Adaptive workspace characterization.

The designed controller ensures that the actual operation commands can be accurately replicated, thereby completing the task precisely and efficiently in various loaded states.

A. Transformed Workspace Setting

As shown in Fig. 1, the slave hydraulic manipulator is configured with only four DOFs, which means the workspaces of the master robot and the manipulator exhibit a low similarity. To facilitate the completion of the master-slave operation, this article defines the transformed workspace, and the dimensions of the transformed workspace are set dependent on the number of DOFs exhibited by the slave hydraulic manipulator.

Given that the first joint of the master robot and the slave manipulator is isomorphic, the first dimension of the transformed workspace (D_1) is defined as the first joint orientation. To make full use of the slave hydraulic manipulator's workspace to ensure the completion of the master-slave operation task in the largest possible range, the remaining DOFs of the slave manipulator should be all used for the end-effector positioning. To this end, the cylindrical coordinate system is used to specify the second (D_2) and third (D_3) dimensions of the transformed workspace. Furthermore, since the slave hydraulic manipulator lacks attitude angle DOFs in two directions, the fourth dimension of the transformed workspace (D_4) is set as the pitch operation attitude angle θ_r around the I-axis, which means the direction of connection between the end point and base of the master robot [29], which is determined by the fourth DOF of the slave manipulator.

B. Adaptive Mapping Scheme

A novel adaptive mapping scheme is developed, which maps the operation command in the master transformed workspace onto the slave transformed workspace to reproduce the operator's intent accurately. Considering that the first joint of the master robot and the slave manipulator are isomorphic, the mapping of D_1 is proportional mapping. Then, the last three dimensions of the transformed workspace (LTTW) are defined and discussed individually in the following parts. In order to present the LTTW more clearly, the master last three-dimensional transformed workspace (m-LTTW) is shown in Fig. 2(a) and the slave last three-dimensional transformed workspace (s-LTTW) is shown in Fig. 2(b).

As the operator governs the master robot directly, the operation command point can be positioned at any location in the master transformed workspace. To depict the operator's operation intention more effectively, the adaptive workspace and the determination index of the mapping scheme are set in m-LTTW. Two spheres within the m-LTTW are established, whose center is the focal point of the m-LTTW, and radii are determined as the positioning radius R_P and the navigation radius R_N. It's noteworthy that these radii (including similar definitions in the following part) refer to the vector composed of the percentage of the maximum area occupied by m-LTTW in D_2-D_4. Then, the m-LTTW can be divided into three areas as shown in Fig. 2(c).

The determination index of the adaptive mapping scheme denoted as the actual operation command radius R_{op}, is defined as the vector from the focal point in the m-LTTW to the actual operation command point. Then, the TWAM final result P_i can be expressed as

$$P_i = P_{obj_P} + (P_{obj_T} - P_{obj_P}) \mathbf{H} (||R_{op}|| - ||R_P||) \\ + (P_{obj_N} - P_{obj_T}) \mathbf{H} (||R_{op}|| - ||R_N||) \tag{1}$$

where $\mathbf{H}$ denotes the Heaviside step function. P_{obj_N}, P_{obj_T}, and P_{obj_P} respectively represent the navigation, transition, and positioning mapping result which will be discussed as follows.

1) Navigation Mapping: Navigation mapping is similar to position-velocity mapping, wherein the maximum three-dimensional motion velocity of s-LTTW $v_{max} = [v_{D_{2max}}, v_{D_{3max}}, v_{D_{4max}}]^T$ is predetermined. The mapping is achieved based on the location of the actual operation command point in the m-LTTW

$$\dot{P}_{obj_N} = (||R_{op}|| - ||R_P||) / (||R_{max}|| - ||R_P||) \cdot v_{max} \tag{2}$$

$$P_{obj_N} = P_{obj} + \dot{P}_{obj_N} \cdot dt \tag{3}$$

where P_{obj} and dt are the initial position of the command point in s-LTTW and the mapping update time, respectively.

Through sending operation command points located within the navigation area, the operator can directly and easily control the manipulator to quickly move within the workspace, thereby maximizing the utilization of the slave workspace.

2) Positioning Mapping: Due to the difference in shape between the elliptical positioning area in m-LTTW and the

irregular polyhedral shape of s-LTTW, the general proportional position-position mapping approach can only guarantee accurate control within a very limited area of s-LTTW, which means the accurate utilization ratio (AUR, the ratios of the accurately teleoperated area in the whole workspace) of the slave workspace is too low. Consequently, a variable-scale one-to-one-axis mapping (VOM) approach that utilizes boundary information of s-LTTW as the transformation basis is developed to enhance the similarity between the mapped space and the s-LTTW, and expand the area that can be accurately teleoperated as much as possible and improve the AUR. The VOM can be summarized as

$$D_{s_i} = \frac{\sigma\left(D_{s_i}^{max} - D_{s_i}^{min}\right) \cdot d_{m_d}}{\|R_P\|} + \frac{D_{s_i}^{max} + D_{s_i}^{min}}{2} \quad (4)$$

where $i = 2,3,4$ is the dimension characterization parameter. d_{m_d} denote the distance between the operating point and the spherical center of the positioning area. The scale factor σ is employed to ensure that all commands after positioning mapping remain within the s-LTTW. $D_{s_i}^{max}$ and $D_{s_i}^{min}$ are the maximum and minimum values of each s-LTTW's axis, which can be determined according to the following step.

The mapping axis order is determined based on the box-counting dimension which can be expressed as

$$\aleph_i = \lim_{\hbar \to 0} \frac{\log N_i(\hbar)}{\log(1/\hbar)} \quad (i = 2,3,4) \quad (5)$$

where $\aleph_i$ represents the fractal dimension of s-LTTW's each axis, $N_i(\hbar_i)$ and $\hbar_i$ denote the number and edge length of covered micro-boxes. The smaller fractal dimension of each axis indicates that the distribution of s-LTTW in the direction of the corresponding axis is approximately linear and straightforward. Based on the fractal dimensions $\aleph_i$, the most direct and indirect spatial distribution of the transformed workspace axis (I^- and I^+) can be determined as

$$I^- = \aleph^{-1}\left(min\left(\aleph_i\right)\right), \quad I^+ = \aleph^{-1}\left(max\left(\aleph_i\right)\right) \quad (6)$$

where $\aleph^{-1}$ represents the correspondence between each fractal dimension and the axes. And the maximum and minimum values of s-LTTW's I^--axis can be directly defined as

$$D_{s_{I^-}}^{max} = \max_{\mathbf{x} \in \mathbf{FL}} \mathbf{x} \cdot \mathbf{d}_{I^-}, \quad D_{s_{I^-}}^{min} = \min_{\mathbf{x} \in \mathbf{FL}} \mathbf{x} \cdot \mathbf{d}_{I^-} \quad (7)$$

where $\mathbf{FL}$ and $\mathbf{x}$ represent the distribution of s-LTTW and the coordinates of the boundary points, respectively. $\mathbf{d}_{I^-}$ denotes the unit vector in the I^--axis direction. After getting $D_{s_{I^-}}^{max}$ and $D_{s_{I^-}}^{min}$, $D_{s_{I^-}}$ can be obtained by (4). Then, the axis other than I^- and I^+ in the transformed workspace is defined as I^*. By calculating the intersection of the line $D_{I^-} = Ds_{I^-}$ and the distribution boundary of s-LTTW in the I^*-I^- plane, the maximum and minimum values of s-LTTW's I^*-axis can be obtained as

$$D_{s_{I^*}}^{min} = \min(\mathbf{x}_{I^*} \in \mathbf{B}_{I^{*-}} \ \& \ D_{I^-} = Ds_{I^-})$$
$$D_{s_{I^*}}^{max} = \min(\mathbf{x}'_{I^*} \in \mathbf{B}_{I^{*-}} \ \& \ D_{I^-} = Ds_{I^-}) \quad (8)$$

where $\mathbf{B}_{I^{*-}}$ denotes the boundary of s-LTTW in the I^*-I^- plane. $\mathbf{x}_{I^*}$ represents the I^*-axis coordinates of the point within

the distribution boundary of s-LTTW in the I^*-I^- plane, and $\mathbf{x}'_{I^*}$ means the I^*-axis coordinates of the point within the distribution boundary except $D_{s_{I^*}}^{min}$. Similar to (8), based on $D_{s_{I^-}}$ and $D_{s_{I^*}}$, the maximum and minimum values of s-LTTW's I^+-axis can be also obtained as

$$D_{s_{I^+}}^{min} = \min(\mathbf{x}_{I^+} \in \mathbf{B}_I \ \& \ D_{I^-} = Ds_{I^-} \ \& \ D_{I^*} = Ds_{I^*})$$
$$D_{s_{I^+}}^{max} = \min(\mathbf{x}'_{I^+} \in \mathbf{B}_I \ \& \ D_{I^-} = Ds_{I^-} \ \& \ D_{I^*} = Ds_{I^*}) \quad (9)$$

where $\mathbf{B}_I$ denotes the boundary of s-LTTW in the transformed workspace. $\mathbf{x}_{I^+}$ represents the I^+-axis coordinates of the point within the distribution boundary of s-LTTW in the transformed workspace, and $\mathbf{x}'_{I^+}$ means the I^+-axis coordinates of the point within the distribution boundary except $D_{s_{I^+}}^{min}$.

Finally, the position mapping result P_{obj_P} can be determined by the mapping result of each s-LTTW's axis based on the VOM.

Remark II.1: As illustrated in the theoretical description of the VOM method, particularly in (7)-(9), it is evident that the designed VOM is based on the distribution (**FL**) and boundary information ($\mathbf{B}_{I^{*-}}$ and $\mathbf{B}_I$) of the slave workspace, rather than the master workspace. This is a fundamental distinction between the designed mapping method and the conventional mapping method.

3) Transition Mapping: The transition mapping method ensures that the mapping command in s-LTTW will not mutate when the operation command is switched from the navigation area to the positioning area. The transition mapping scheme can be expressed as

$$P_{obj_T} = \left(\alpha_T \cdot P_{N_T} + \beta_T \cdot P_{P_T}\right) / \left(\|R_N\| - \|R_P\|\right) \quad (10)$$

where $\alpha_T = \|R_N\| - \|R_{op}\|$, $\beta_T = \|R_{op}\| - \|R_P\|$. P_{N_T} and P_{P_T} represent the operation command through navigation mapping and positioning mapping at this time, respectively.

Remark II.2: Through the TWAM, the workspace of the slave manipulator can be fully utilized, and the similarity between the mapped workspace and s-LTTW is maximized. Thus, the slave hydraulic manipulator can accurately reproduce the operator's intentions and complete the operation in the largest possible workspace while eliminating the influence of master-slave heterogeneity.

III. NONLINEAR CONTROLLER DESIGN FOR SLAVE HYDRAULIC MANIPULATOR

In this section, the dynamic model-based DIARC is designed to achieve high-precision control of the slave hydraulic manipulator in various loaded states, thereby ensuring the performance of the master-slave operation.

A. Modeling of Hydraulic Manipulator

The nonlinear controller designed herein will be implemented on a common n-DOF hydraulic manipulator, as illustrated in Fig. 3. Each rotary joint of this manipulator is actuated by a hydraulic cylinder that is controlled by a proportional
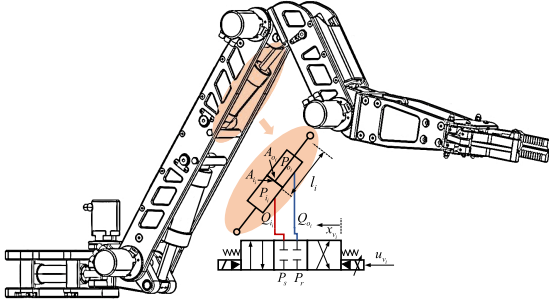
Fig. 3. Typical schematic diagram of a multi-DOF hydraulic manipulator.

valve. The dynamics of an n-DOF general manipulator can be modeled as

$$M_j(q)\ddot{q} + C_j(q,\dot{q})\dot{q} + G_j(q) = \tau - T_f + \Delta_d + \tilde{\Delta}_j \quad (11)$$

where q, $\dot{q}$, and $\ddot{q}$ represent the joint position, velocity, and acceleration, respectively. $M_j(q)$, $C_j(q,\dot{q})$, and $G_j(q)$ are the symmetric positive definite inertia matrix, the centripetal and Coriolis torque, and the gravitational torque, respectively. It is worth noting that since the object of dynamic modeling is the multijoint manipulator, each matrix contains coupling terms formed by each joint angle. τ is the joint driving torque. $T_f = S_f(\dot{q})f_c + \dot{\mathbf{q}}f_v$ is the friction torque of the hydraulic cylinder, with f_c and f_v being the Coulomb friction coefficient and the viscous friction coefficient, respectively. $\dot{\mathbf{q}} \triangleq diag[\dot{q}]$ and $S_f(\dot{q})$ is the Coulomb friction function. Δ_d denote the nominal modeling error and $\tilde{\Delta}_j$ represents the modeling error deviation which also includes uncertain nonlinearities.

The joint driving torque of hydraulic manipulators is generated by the cylinder pressure, so τ can be modeled as

$$\tau = J_j(q)P_L, \quad P_L = A_1 P_1 - A_2 P_2 \quad (12)$$

where $J_j(q)$ is the nonsingular joint Jacobian matrix which contains nonlinear joint coupling effects. P_L is the an intermediate term that facilitates the design of subsequent reduced order controllers. P_1 and P_2 represent the pressures of the rod and rodless cavity of each cylinder. A_1 and A_2 are the diagonal matrix of corresponding piston areas.

Then, the pressure dynamics of the cylinder is modeled as

$$V_1\dot{P}_1/\beta_e = -A_1 J_j(q)\dot{q} + k_{q_1} g_1(P_1, x_v) x_v + \Delta_{Q_1} + \tilde{Q}_1$$
$$V_2\dot{P}_2/\beta_e = A_2 J_j(q)\dot{q} - k_{q_2} g_2(P_2, x_v) x_v - \Delta_{Q_2} - \tilde{Q}_2 \quad (13)$$

where V_1 and V_2 represent the total volumes of the head end and rod end chambers, respectively. β_e is the bulk modulus of the hydraulic oil, which can be treated as a constant. Δ_{Q_1} and Δ_{Q_2} represent the nominal flow discrepancies of the rod and rodless cavities. $\tilde{Q}_1$ and $\tilde{Q}_2$ are the fast time-varying flow uncertain nonlinearities of the rod and rodless cavities. k_{q_1} and k_{q_2} are the flow gain coefficients of the proportional valves. $g_1(P_1, x_v)$ and $g_2(P_2, x_v)$ are the nonlinear flow gain function of the proportional valves. $x_v = k_v u_v$ represents the value opening stroke, where k_v and u_v are the proportionality coefficient of valves and the valve control signal, respectively.

In addition, the end-load disturbance is mainly reflected in each dynamic matrix, namely

$$M_j(q) = M_H(q) + M_L(q)m_L$$
$$C_j(q,\dot{q}) = C_H(q,\dot{q}) + C_L(q)m_L$$
$$G_j(q) = G_H(q) + G_L(q)m_L. \quad (14)$$

Then, the dynamics established as (11) can be optimized as

$$M_H\ddot{q} + C_H\dot{q} + G_H + L_m m_L = \tau - T_f + \Delta_d + \tilde{\Delta}_j \quad (15)$$

where L_m denotes the lumped dynamics of the end-load as follows:

$$L_m(q,\dot{q},\ddot{q}) = M_L(q)\ddot{q} + C_L(q,\dot{q})\dot{q} + G_L(q). \quad (16)$$

B. Model Parameterization

It is necessary to select a set of dynamics parameters that cannot be accurately identified for the purpose of designing subsequent online adaptive laws. For the jth joint, its single joint parameter set ϖ_j is selected as

$$\varpi_j = \left[f_{cj}, f_{vj}, \Delta_{d_j}, \Delta_{Q_{1_j}}, \Delta_{Q_{2_j}}\right]^T \in R^5. \quad (17)$$

The selected parameter set can be divided into the joint parameter set ϑ_j and the overall system parameter set ϑ_s as

$$\vartheta_j = \left[\theta_1^T, \theta_2^T, \theta_3^T, \theta_4^T, \theta_5^T\right]^T \in R^{5n}$$
$$\vartheta_s = [\theta_6, \theta_7]^T = \left[\beta_e^{-1}, m_L\right]^T \in R^2 \quad (18)$$

in which $\theta_i = [\varpi_1(i) \dots \varpi_j(i) \dots \varpi_n(i)]^T$. $\varpi_j(i)$ denotes the ith element of the jth single joint parameter set ϖ_j. So, the final designed key parameter set $\vartheta \in R^{5n+2}$ can be given as

$$\vartheta = \left[\vartheta_j^T, \vartheta_s^T\right]^T. \quad (19)$$

Then, the whole dynamic model can be parameterized as

$$M_H\ddot{q} + C_H\dot{q} + G_H = J_j P_L + \tilde{\Delta}_j - S_f\theta_1 - \dot{\mathbf{q}}\theta_2 + \theta_3 - L_m\theta_7$$
$$\dot{P}_L\theta_6 = -J_j\zeta_{Q3}\dot{q} + Q_L + \tilde{\Delta}_Q + \zeta_{Q1}\theta_4 + \zeta_{Q2}\theta_5 \quad (20)$$

where $Q_L = \left(\zeta_{Q1}k_{q_1}g_1 + \zeta_{Q2}k_{q_2}g_2\right)x_v$, $\zeta_{Q1} = A_1 V_1^{-1}$, $\zeta_{Q2} = A_2 V_2^{-1}$, $\zeta_{Q3} = A_1^T V_1^{-1} A_1 + A_2^T V_2^{-1} A_2$, and $\tilde{\Delta}_Q = \zeta_{Q3}\tilde{Q}_1 + \zeta_{Q4}\tilde{Q}_2$.

C. Nonlinear Controller Design

In this section, the backstepping method is introduced to cope with the high-order characterize of hydraulic manipulator dynamics, and the direct/indirect adaptive robust control method which shown in Fig. 4 is proposed to decrease the impact of uncertain nonlinear factors and end-load disturbance.

The following notations are used throughout this article: $\hat{\bullet}$ denotes the estimation of $\bullet$, and $\tilde{\bullet} = \hat{\bullet} - \bullet$. $\bullet_f$ means the filtering result of $\bullet$.

STEP I:

Define $z_1 = q - q_d$ and the sliding-mode-like error z_2 as

$$z_2 = \dot{q} - \dot{q}_{eq}, \quad \dot{q}_{eq} \triangleq \dot{q}_d - k_1 z_1 \quad (21)$$
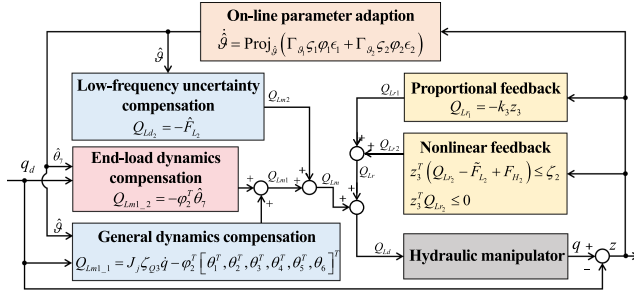
Fig. 4.   Diagram of the designed DIARC.

where k_1 is a positive gain matrix, and q_d is the target trajectory. The frequency domain conversion relation between z_2 and z_1 can be written as $G(s) = 1/(k_1 + s)$, which means z_1 will be very small or converge to zero, as long as $z_2 \to 0$.

According to (20) and (21), we can obtain as follows:

$$M_H \dot{z}_2 + C_H z_2 = J_j P_{Ld} + J_j z_3 + \varphi_1^T \vartheta - \xi_H + \tilde{\Delta}_j \quad (22)$$

in which $\varphi_1^T = [-S_f, -\dot{\mathbf{q}}, \mathbf{I}_n, \mathbf{0}_n, \mathbf{0}_n, \mathbf{0}_n, L_m]$, $z_3 = P_L - P_{Ld}$, and $\xi_H = M_H \ddot{q}_{eq} + C_H \dot{q}_{eq} + G_H$.

The control law P_{Ld} in **STEP I** can be designed as

$$P_{Ld} = P_{Lm_1} + P_{Lr_1} + P_{Lm_2} + P_{Lr_2}$$
$$P_{Lm_1} = -J_j^{-1} \varphi_1^T \hat{\vartheta} + \xi_H, \quad P_{Lr_1} = -k_2 z_2 \quad (23)$$

where k_2 is a positive gain matrix. Furthermore, the uncertainty arising from the modelling uncertainty and parameter estimation error can be divided into a low-frequency part F_{L_1} and a high-frequency time-varying part F_{H_1}, that is as follows:

$$F_{L_1} + F_{H_1} \triangleq -\varphi_1^T \tilde{\vartheta} + \tilde{\Delta}_j. \quad (24)$$

For coping with the abovementioned low-frequency dynamics deviation F_{L_1}, P_{Lm_2} is designed as $P_{Lm_2} = J_j^{-1} \hat{F}_{L_1}$, where $\hat{F}_{L_1}$ can be determined by

$$\dot{\hat{F}}_{L_1} = \begin{cases} 0, & \text{if } \left| \hat{F}_{L_1} \right| = F_{LB_1} \ \& \ \hat{F}_{L_1} z_2 > 0 \\ \gamma_1 z_2, & \text{else} \end{cases} \quad (25)$$

where γ_1 is the positive constant gain, and F_{LB_1} denotes the known boundary of F_{L_1}. Then, the nonlinear feedback term P_{Lr_2} is designed to satisfy the following unequal conditions:

$$z_2^T \left(J_j P_{Lr_2} - \tilde{F}_{L_1} + F_{H_1} \right) \leq \zeta_1 \ \& \ z_2^T J_j P_{Lr_2} \leq 0 \quad (26)$$

with ζ_1 being a designed infinitesimal parameter.

STEP II:

The error dynamics of z_3 can be summarized as

$$\dot{P}_L \theta_6 = -J_j \zeta_{Q3} \dot{q} + Q_L + \varphi_2^T \vartheta + \tilde{\Delta}_Q - \dot{P}_{Ld_u} \theta_6$$
$$\dot{P}_{Ld_u} = \dot{P}_{Ld} - \dot{P}_{Ld_c} \quad (27)$$

in which $\varphi_2^T = [\mathbf{0}_n, \mathbf{0}_n, \mathbf{0}_n, \zeta_{Q1}, \zeta_{Q2}, -\dot{P}_{Ld_c}, \mathbf{0}_n]$. $\dot{P}_{Ld_u}$ and $\dot{P}_{Ld_c}$ denote the incalculable and calculable part of $\dot{P}_{Ld}$, respectively.

And the control law Q_{Ld} in **STEP II** is given by

$$Q_{Ld} = Q_{Lm_1} + Q_{Lr_1} + Q_{Lm_2} + Q_{Lr_2}$$

$$Q_{Lm_1} = J_j \zeta_{Q3} \dot{q} - \varphi_2^T \hat{\vartheta}, \quad Q_{Lr_1} = -k_3 z_3. \quad (28)$$

Similar to (24), define

$$F_{L_2} + F_{H_2} \triangleq -\varphi_2^T \tilde{\vartheta} + \tilde{\Delta}_Q - \dot{P}_{Ld_u} \theta_6. \quad (29)$$

Then, Q_{Ldm_2} is designed as $Q_{Ld_2} = -\hat{F}_{L_2}$, where $\hat{F}_{L_2}$ is the estimation of F_{L_2} which is determined by

$$\dot{\hat{F}}_{L_2} = \begin{cases} 0, & \text{if } \left| \hat{F}_{L_2} \right| = F_{LB_2} \ \& \ \hat{F}_{L_2}(t) z_3 > 0 \\ \gamma_2 z_3, & \text{else} \end{cases} \quad (30)$$

where γ_2 is the positive constant gain, and F_{LB_2} denotes the known boundary of F_{L_2}. Then, the nonlinear feedback term Q_{Lr_2} is designed to satisfy the following unequal conditions:

$$z_3^T \left(Q_{Lr_2} - \tilde{F}_{L_2} + F_{H_2} \right) \leq \zeta_2 \ \& \ z_3^T Q_{Lr_2} \leq 0 \quad (31)$$

in which ζ_2 is a designed infinitesimal parameter.

Finally, the actual control output u_{v_d} is given by

$$u_{v_d} = k_v^{-1} \left(\zeta_{Q1} k_{q_1} g_1 + \zeta_{Q2} k_{q_2} g_2 \right)^{-1} Q_{Ld}. \quad (32)$$

Afterward, a parameter adaptive law based on estimation error was introduced to further address the parameter uncertainties. Ignoring the uncertain nonlinearities of hydraulic manipulator dynamics, the linear regression equation for ϑ can be written as $u_{si} = -\varphi_{si}^T \vartheta, \ (i = 1, 2)$, where

$$u_{s1} = M_H \ddot{q} + C_H \dot{q} + G_H - J_j P_L$$
$$u_{s2} = Q_L - J_j \zeta_{Q3} \dot{q} \quad (33)$$

with $\varphi_{s1} = \varphi_1$ and $\varphi_{s2} = [\mathbf{0}_n, \mathbf{0}_n, \mathbf{0}_n, \zeta_{Q1}, \zeta_{Q2}, -\dot{P}_d, \mathbf{0}_n]$.

By utilizing the filter $H_{f1} = 1/(\tau_f s + 1)$ and $H_{f2} = s/(\tau_f s + 1)$, the system estimated error can be written as

$$\epsilon_i = -\varphi_{si_f} \hat{\vartheta} - u_{s_{i_f}}. \quad (34)$$

And the parametric adaptive law is set as

$$\dot{\hat{\vartheta}} = \text{Proj}_{\hat{\vartheta}} \left(\Gamma_{\vartheta_1} \varsigma_1 \varphi_1 \epsilon_1 + \Gamma_{\vartheta_2} \varsigma_2 \varphi_2 \epsilon_2 \right) \quad (35)$$

where the projection $\text{Proj}_{\hat{\vartheta}}$ is a projection mapping [30]. Γ_{ϑ} and ς are the adaptation gain and adjustment index which is summarized as

$$\dot{\Gamma}_{\vartheta_i} = \begin{cases} \varepsilon_i \Gamma_{\vartheta_i} - \varsigma_i \Gamma_{\vartheta_i} \varphi_i \varphi_i^T \Gamma_{\vartheta_i}, & \text{if } \Gamma_{\vartheta_i}(t) \leq \rho_{max} \mathbf{I} \\ 0, & \text{otherwise} \end{cases} \quad (36)$$

with $\varsigma_i = 2 \left(1 + \nu \varphi_i^T \Gamma_{\vartheta_i} \varphi_i \right)^{-1}$. $\varepsilon_i \leq 1$ and $\nu \geq 0$ are the forgetting and insurance factor for adaptation, respectively. ρ_{max} represents the upper bound of adaptive updating law.

Then, the following theorems can be drawn.

Theorem III.1: All signals in closed-loop control system of hydraulic manipulator are bounded. ∎

Theorem III.2: After a finite time, in the presence of parametric uncertainties only, the model parameter can converge to the true values, that is, $\tilde{\vartheta} \to 0$ under the condition of continuous excitation which can be drawn as

$$\int_{t-T}^{t} \varphi_{si_f} \varphi_{si_f}^T \, d\tau_i \geq \beta_i I, \quad \forall t > t_0. \quad (37)$$

Furthermore, the asymptotic output tracking (or zero final tracking error) can be achieved, i.e., $z_1 \to 0$ as time $\to \infty$. ∎

This article has been accepted for inclusion in a future issue of this journal. Content is final as presented, with the exception of pagination.

ZHOU et al.: TWAM BASED MASTER-SLAVE OPERATION CONTROL
7

Fig. 5. Configuration of the master and slave devices.

TABLE I
DH PARAMETERS OF THE MASTER AND SLAVE DEVICES

	Master Robot				Slave Manipulator			
	q	d	a(mm)	$\alpha(°)$	q	d	a(mm)	$\alpha(°)$
Joint1	q_{1m}	0	0	0	q_1	0	90	0
Joint2	q_{2m}	0	35	90	q_2	0	605	90
Joint3	q_{3m}	0	152	0	q_3	0	290	0
Joint4	q_{4m}	0	138	−90	q_4	0	285	0
Joint5	q_{5m}	0	0	90				
Joint6	q_{6m}	0	0	−90				

IV. EXPERIMENT AND ANALYSIS

A. Experimental Setup

A real-time system in MATLAB/Simulink with a communication loop operating at 1 kHz between the master and slave manipulators is implemented to conduct the experiment, and the configuration of the master robot and the slave manipulator is shown in Fig. 5.

The master device, named Phantom Omni, is a 6-DOFs passive robot equipped with angle and torque sensors. It is a closed-source commercial product. The device is capable of providing both the end pose and joint angles of each manipulator joint, while also exerting torque feedback for the first three joints. In this article, the master robot is employed to send the operator's commands and to feedback the joint torques, which are reconstructed by the joint angle of the slave manipulator transmitted back to the master side during the operation.

The slave hydraulic manipulator is a 4-DOFs manipulator equipped with general joint angle sensors (Melexis MLX90316) and pressure sensors (Gefran KSE-E-ZB160). The core proportional valve selected is the Bosch Rexroth 4WRPEH, which responds to an analogue signal input, allows for a maximum working pressure of 35 MPa, and operates at a rated flow rate of 40 l/min. The hydraulic pump selected is a constant displacement gear pump with a rated flow rate of 12 L/min. Moreover, the dimensions and stroke lengths of the hydraulic cylinders at each joint are not consistent due to the varying lengths and weights of the hydraulic manipulator's linkages. The diameter of the hydraulic cylinder at joint1 is 32 mm, with a stroke length of 80 mm. The cylinder at joint2 has a diameter of 50 mm and a stroke length of 104 mm. The cylinder at joint3 has a diameter of 40mm and a stroke length of 82 mm. Finally, the cylinder at joint4 has a diameter of 32mm and a stroke length of 62mm.

Furthermore, to provide a more intuitive illustration of the master-slave heterogeneity of the experimental platform, the DH parameters of the master and slave manipulator are presented as Table I (q_{im} represents the angle that the i-th joint of the master robot has rotated through under the control of the operator). Then, three experiments are set as follows.

Set 1 : Mapping Experiment.

The operating command operation point set located within the m-LTTW positioning area (which requires accurate operation) is prepared, and mapped to the control target position point set of the slave hydraulic manipulator by the traditional PPM with small (**M1**) and large (**M2**) scaling factors, as well as the proposed TWAM method (**M3**), respectively. Given that the actual operational quality is depending upon not only the

mapping accuracy but also the control precision, the main purpose of this experiment is to verify the performance of command mapping methods with effectively excluding the impact of control precision.

The operating command operation point set is obtained by uniformly sampling points within the positioning area. The reason for utilizing it as an input for the command mapping method in SET 1 is that by presetting the operating command points that are distributed throughout the positioning area, the mapped points can be obtained from the command mapping method. By comparing the results of the command mapping method at various locations within the positioning area, the proportion and similarity of the mapped workspace when the positioning area is fully utilized (the operating command point set is distributed uniformly throughout the positioning area) to the actual slave workspace can be analyzed.

As for the predetermined radii R_P and R_N, the half-axis vector in each dimension of the m-LTTW's maximum inscribed ellipsoid can be calculated as: $\mathbf{L2} = [l2, 0, 0]$, $\mathbf{L3} = [0, l3, 0]$, and $\mathbf{L4} = [0, 0, l4]$, where $l2$, $l3$, and $l4$ are the half axis length of each dimension, and R_P and R_N are set as $R_P = 0.6(\mathbf{L2} + \mathbf{L3} + \mathbf{L4})$, $R_N = 0.7(\mathbf{L2} + \mathbf{L3} + \mathbf{L4})$.

Set 2 : Grasp Experiment.

The hydraulic manipulator was teleoperated to grasp three underwater targets of varying positions and weights and place them on the designated underwater platform (as shown in Fig. 6) based on the common-used PID controller (**C1**), the controller proposed in our previous work [30] (**C2**) and the designed controller (**C3**). It is noteworthy that the experimental results presented in [30] have demonstrated that **C2**, in comparison to other commonly used nonlinear controller, achieves better control accuracy. Consequently, it can be inferred that if the controller designed in this article achieves improved control accuracy compared to **C2**, it will inevitably demonstrate better performance than other commonly used nonlinear controller. This experiment aims to validate the feasibility and effectiveness of the TWAM-based master-slave operation control for hydraulic manipulators.

The main coefficients of each controller are as follows:
C1: The gain coefficients are tuned according to the standard step of PID turning, and the final coefficients is given as: $K_P = diag([110, 130, 115, 80])$, $K_I = diag([12, 22, 23, 16])$ and $K_D = diag([1.2, 1.6, 2.3, 2.2])$.
C2: Referring to the gain coefficients of PID and adjusting accordingly, the key coefficients are set as: $k_1 = diag([70, 85, 80, 100])$, $k_2 = diag([90, 70, 40, 20])$,
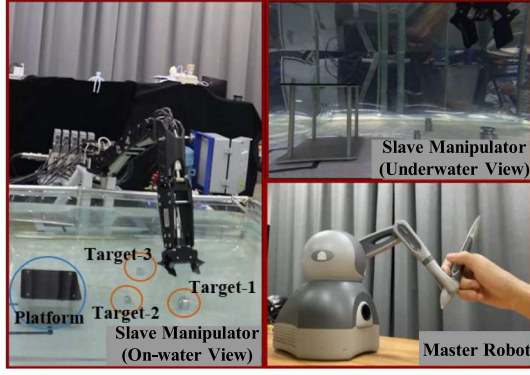
Fig. 6.   Real-time experimental platform.

Fig. 7.   Mapping experiment results.

$k_3 = diag([70, 100, 150, 130])$, $\gamma_1 = diag([220, 150, 100, 80])$, and $\gamma_2 = diag([2, 1, 5, 6]) \times 10^{-8}$.

C3: It is also noteworthy that the structures of **C2** and **C3** are highly similar, and the basic gain coefficients and model parameter adaptive coefficients of **C2** and **C3** are consistent. The key difference between the two controllers is that **C3** additionally considers the end-load disturbance.

Set 3 : **Heavy-loaded Experiment**.

The hydraulic manipulator with heavy end load $(20kg)$ is controlled by **C2** and **C3** to track the desired trajectory. The purposed of **Set 3** is to evaluate the performance of the designed DIARC in occasions involving heavy loads and power augmentation, which are the common application for hydraulic systems. And to highlight the impact of heavy loads on control performance, the desired trajectory and control parameters are set consistent with those employed in **Set 2**.

B. Mapping Experiment Results

The mapping experiment results are shown in Fig. 7 and Table II. The left subplots illustrate that the traditional PPM with a small scaling factor. The results demonstrate that a smaller scaling factor is associated with a narrower mapped workspace to prevent exceeding the boundaries of the slave workspace. However, this also results in a low AUR (the ratio between the blue and the red region in Fig. 7) of the slave workspace, which can lead to the manipulator being unable to reach a part of the slave workspace, thereby affecting the actual operational effectiveness. In contrast, the middle subplot illustrates the PPM with a larger scaling factor, indicating that a larger scaling factor can more effectively increase the AUR, although some of the mapped commands exceed the boundaries of the slave workspace. This leads to the possibility of exceeding the joint limits of the manipulator during operation, which could also impact the operational effectiveness. Conversely, due to that the VOM is based on the distribution and boundary of the slave workspace, the mapping results for **M3** presented in the right subplots achieve a large AUR within in the slave workspace, which means the proposed mapping method provides a good balance of high precision utilization and low risk of exceeding the boundaries of slave workspaces.
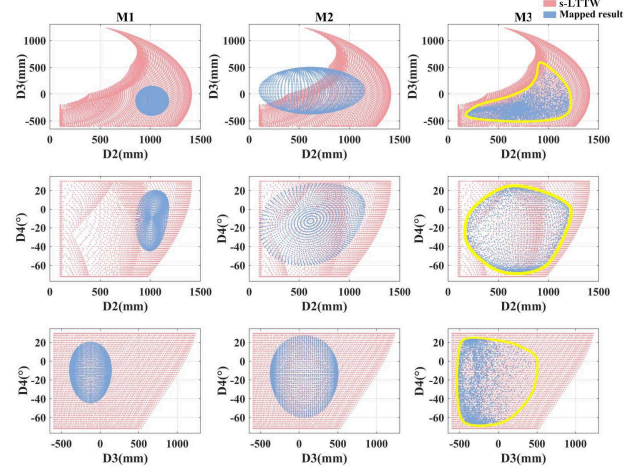
TABLE II
RESULTS OF MAPPING EXPERIMENT

	AUR	HDD	Exceeding Boundary?
M1	21.3%	117.54 mm	No
M2	65.9%	93.31 mm	Yes
M3	68.8%	25.45 mm	No

Moreover, to evaluate the similarity of the mapped space and the slave workspace more professional, the authors introduced the Hausdorff distance in the field of image processing, which is calculated as

$$\mathbf{HDD}_i = \max\{\mathbf{h}(\text{Mapped}_i), \mathbf{FL}), \mathbf{h}(\mathbf{FL}, \text{Mapped}_i)\}$$

$$\mathbf{h}(A, B) = \max_{a \in A} \left\{ \min_{b \in B}\{d(a, b)\} \right\} \tag{38}$$

where **FL** and Mapped_i represent the distribution of slave workspace and mapped space obtained by Mi.

According to the HDD shown in Table II, it can be found that the mapped spaces of **M1** and **M2** both exhibit a low similarity with the slave workspace. This suggests that the relative positioning of the mapped commands within the slave workspace is significantly dissimilar to that of the operator's commands within the master workspace. Consequently, the reproduction of the operator's intent is constrained. In contrast, as the VOM in TWAM is based on the distribution and boundary of the slave workspace, the mapped space obtained by TWAM maintains a high similarity with the slave workspace, which is beneficial for accurately reproducing the operator's intent.

C. Grasp Experiment Results

The experiment video is available in the supplementary material. During the whole process, the mapping phase of this experiment, unlike **Set 1**, not only involved positioning mapping, but also comprehensively examines the entire TWAM algorithm. The mapping result during the whole process is shown as Fig. 8. When the operator sends commands by Omni, R_{op} is calculated and compared with R_N and R_P to determine the mapping
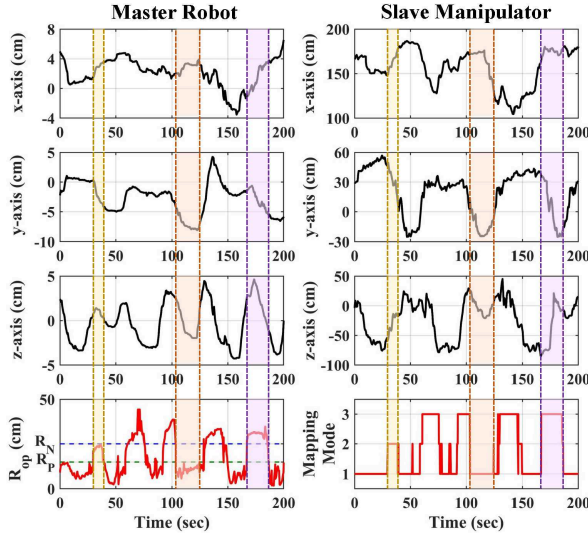
Fig. 8. Grasp experimental mapped results.

Fig. 9. Grasp experimental control results.

Fig. 10. Heavy-loaded experiment results.

mode (1, 2, and 3 represent positioning, transition, and navigation mapping, respectively). During the positioning mapping (e.g. orange area), the mapped point precisely replicates the operator's intent to achieve accurate operations. The navigation mapping (e.g., purple area), on the other hand, involves quick traversal of the manipulator's workspace to achieve rapid movement. Finally, transition mapping (e.g., yellow area) provides a smooth transition from the mapped point, avoiding manipulator chattering.

The control results of the hydraulic manipulator are illustrated in Fig. 9, and the specific control performance indexes are shown in Table III. It is noteworthy that all control parameters used in this article have been optimally tuned, as reflected by the critical oscillations observed in the steady-state tracking of each joint of the manipulator. It can be seen from Fig. 9 that PID controller, which ignores the complex dynamics of hydraulic manipulator, can only achieve limited precision. Furthermore, the results demonstrate that the manipulator controlled by **C3** achieved joint space error within $2°$. It is noteworthy that throughout the experiment, the hydraulic manipulator repeatedly performed the actions of positioning, gripping, and placing different targets, indicating that its end-load states were always changing. In this case, the **C3**-controlled manipulator was able to achieve stable operation with little change in control accuracy due to the end-load disturbance compensation. Furthermore, **C2**, which exhibits a near-identical control structure to that of C3 but does not incorporate the end-load disturbance additionally, achieves similar control accuracy of joint-1 to **C3** due to the motion of joint-1 being load-independent. However, in other control result, the precision of **C2** is always unsatisfactory given that the hydraulic manipulator is operating with time-varying end-load states, which means that **C2** is difficult to compensate for the influence caused by various end-load disturbance compared with **C3**. The remarkable control accuracy achieved by **C3** can ensure the successful task execution of
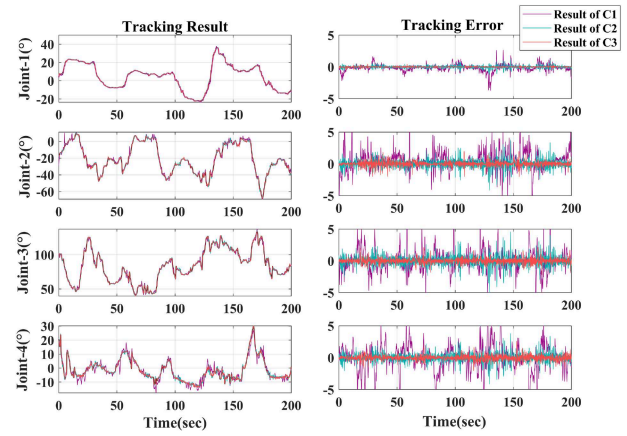
hydraulic manipulators such as positioning, grasping, or movement toward the vicinity of the target.

Besides, by analyzing the motion range percentage shown in Table III, it is clear that the proposed method maximizes the use of the slave workspace, thereby enabling the manipulator to complete various master-slave operation tasks within the largest possible range of workspace.

D. Heavy-loaded Experiment Results

Furthermore, it is important to note that all underwater targets in the grasping experiment have been purposefully selected to be markedly small. Nevertheless, this does not indicate that these experiments are inconsistent with the practical applications of hydraulic systems. Although hydraulic systems are frequently employed where heavy loads and power augmentation

TABLE III
CONTROL RESULTS OF GRASP EXPERIMENT

	Peak Error(°)			RMSE(°)			Range Percentage
	C1	C2	C3	C1	C2	C3	C1&C2&C3
Joint1	3.72	1.22	0.48	0.54	0.18	0.07	81.86%
Joint2	9.66	4.17	1.77	1.45	0.58	0.33	68.92%
Joint3	8.17	5.01	2.25	1.58	0.69	0.35	77.69%
Joint4	6.31	4.17	1.60	1.97	0.58	0.35	74.95%

This article has been accepted for inclusion in a future issue of this journal. Content is final as presented, with the exception of pagination.

10   IEEE TRANSACTIONS ON INDUSTRIAL ELECTRONICS

TABLE IV
CONTROL RESULTS OF HEAVY-LOADED EXPERIMENT

	Peak Error of C2(°)			Peak Error of C3(°)		
	Set 2	Set 3	Relative Variation	Set 2	Set 3	Relative Variation
Joint1	1.22	1.27	4.10%	0.48	0.50	4.17%
Joint2	4.17	15.19	264.27%	1.77	2.28	28.81%
Joint3	5.01	12.67	152.89%	2.25	2.27	0.89%
Joint4	4.17	10.27	146.28%	1.60	1.73	8.13%

are required, as previously discussed in Section I, hydraulic manipulators have been increasingly applied in the high-precision operation. The purpose of setting the underwater targets to be small is to meet this requirement, which minimizing the allowable control error and heightening the precision requirements during grasping. However, it noteworthy that the designed controller is not limited to these applications. Conversely, it can be applied to broader scenarios, such as those involving heavy loads and power augmentation. To illustrate the versatility of the controller, **Set 3** is conducted, and the results are shown in Fig. 10 and Table IV.

The results demonstrate that even with heavy-load conditions, **C3**, which considers the dynamic disturbances caused by the end-load, can maintain similar control accuracy as that achieved under light-load or no-load conditions. Conversely, the control accuracy of **C2** is significantly reduced as the end-load increases. The experimental results illustrate that the designed controller is effective in achieving precise control of the hydraulic manipulator in varying end-load conditions, which is highly significant for the utilization of hydraulic manipulators in heavy-load precision operation scenarios.

V. CONCLUSION

This article proposed a TWAM-based master-slave operation control scheme for hydraulic manipulators. To unify the dimensions of the master and slave workspaces, a novel coordinate system definition is proposed to establish a transformed workspace, and the impact of master-slave heterogeneity is significantly eliminated by introducing an adaptive command mapping approach. Specifically, the positioning mapping based on the VOM is designed to improve the similarity between the mapped space and the slave workspace, as well as the accurate utilization of the slave workspace. This approach guarantees the accurate reproduction of the operator's intent within the largest possible slave workspace. Moreover, the navigation mapping is proposed to fully traverse the slave workspace, thereby enhancing the efficiency of the master-slave operation. Based on the accurate reproduction of the operator's intent, a DIARC with end-load disturbance compensation is designed to ensure precise control under the complex dynamics of hydraulic manipulators and the varying end-load states, ultimately achieving optimal master-slave operation of hydraulic manipulators. The effectiveness of the proposed TWAM approach and DIARC is verified through numerous comparative experiments. Furthermore, based on the proposed scheme, the master-slave precise grasping in water, which is the typical application of hydraulic manipulators, is achieved. This study holds promising practical

value for hydraulic manipulators in high-precision master-slave control-dependent operations such as underwater sampling. In the future, the operational force feedback and visual guidance assistance will be investigated and integrated with the proposed scheme to realize more immersive master-slave operation of hydraulic manipulators. Furthermore, experiments will be conducted in a lake environment with a fine-sealing hydraulic manipulator to verify the operational performance in harsher situations.

REFERENCES

[1] F. Zhang, J. Zhang, M. Cheng, and B. Xu, "A flow-limited rate control scheme for the master–slave hydraulic manipulator," *IEEE Trans. Ind. Electron.*, vol. 69, no. 5, pp. 4988–4998, May 2022.

[2] N. Tan, P. Yu, M. Zhang, and C. Li, "Toward unified adaptive teleoperation based on damping ZNN for robot manipulators with unknown kinematics," *IEEE Trans. Ind. Electron.*, vol. 70, no. 9, pp. 9227–9236, Sep. 2023.

[3] Y. Fu, W. Lin, X. Yu, J. J. Rodriguez-Andina, and H. Gao, "Robot-assisted teleoperation ultrasound system based on fusion of augmented reality and predictive force," *IEEE Trans. Ind. Electron.*, vol. 70, no. 7, pp. 7449–7456, Jul. 2023.

[4] Y. Lin, Z. Chen, and B. Yao, "Unified motion/force/impedance control for manipulators in unknown contact environments based on robust model-reaching approach," *IEEE/ASME Trans. Mechatron.*, vol. 26, pp. 1905–1913, Aug. 2021.

[5] J. Zhang et al., "Development of a virtual platform for telepresence control of an underwater manipulator mounted on a submersible vehicle," *IEEE Trans. Ind. Electron.*, vol. 64, no. 2, pp. 1716–1727, Feb. 2017.

[6] S. Sivcev, J. Coleman, E. Omerdić, G. Dooly, and D. Toal, "Underwater manipulators: A review," *Ocean Eng.*, vol. 163, pp. 431–450, Sep. 2018.

[7] S. Sakaino, T. Furuya, and T. Tsuji, "Bilateral control between electric and hydraulic actuators using linearization of hydraulic actuators," *IEEE Trans. Ind. Electron.*, vol. 64, pp. 4631–4641, Jun. 2017.

[8] C. Yang, Y. Zhang, Y. Zhao, and L. Cheng, "Human-robot shared control system based on 3D point cloud and teleoperation," *Sci. China Technol. Sci.*, vol. 66, pp. 2406–2414, Apr. 2023.

[9] H. Shen and Y.-J. Pan, "Improving tracking performance of nonlinear uncertain bilateral teleoperation systems with time-varying delays and disturbances," *IEEE/ASME Trans. Mechatron.*, vol. 25, no. 3, pp. 1171–1181, Jun. 2020.

[10] L. Wan and Y.-J. Pan, "Bilateral teleoperation of a multi-robot formation with time-varying delays using adaptive impedance control," in *Proc. IEEE/ASME Int. Conf. Adv. Intell. Mechatron. (AIM)*, 2022, pp. 1739–1746.

[11] Q. Liao, D. Sun, and H. Andreasson, "FuzzyPSReg: Strategies of fuzzy cluster-based point set registration," *IEEE Trans. Robot.*, vol. 38, no. 4, pp. 2632–2651, Aug. 2022.

[12] D. Sun, Q. Liao, and A. Loutfi, "Type-2 fuzzy model-based movement primitives for imitation learning," *IEEE Trans. Robot.*, vol. 38, no. 4, pp. 2462–2480, Aug. 2022.

[13] G. Li, F. Caponetto, E. Del Bianco, V. Katsageorgiou, I. Sarakoglou, and N. G. Tsagarakis, "Incomplete orientation mapping for teleoperation with one DoF master-slave asymmetry," *IEEE Robot. Automat. Lett.*, vol. 5, no. 4, pp. 5167–5174, Oct. 2020.

[14] G. Li, F. Caponetto, X. Wu, and N. G. Tsagarakis, "A haptic shared autonomy with partial orientation regulation for dof deficiency in remote side," *IEEE Trans. Haptics*, vol. 16, no. 1, pp. 86–95, Jan./Mar. 2023.

[15] F. Huang, X. Chen, Z. Chen, and Y.-J. Pan, "A novel SMMS teleoperation control framework for multiple mobile agents with obstacles avoidance by leader selection," *IEEE Trans. Syst., Man, Cybern.: Syst.*, vol. 53, no. 3, pp. 1517–1529, Mar. 2023.

[16] Z. Chen, F. Huang, C. Yang, and B. Yao, "Adaptive fuzzy backstepping control for stable nonlinear bilateral teleoperation manipulators with enhanced transparency performance," *IEEE Trans. Ind. Electron.*, vol. 67, no. 1, pp. 746–756, Jan. 2020.

[17] Z. Chen, S. Zhou, C. Shen, L. Lyu, J. Zhang, and B. Yao, "Observer-based adaptive robust precision motion control of multi-joint hydraulic manipulator," *IEEE/CAA J. Automatica Sinica*, vol. 11, no. 5, pp. 1213–1226, May 2024.

This article has been accepted for inclusion in a future issue of this journal. Content is final as presented, with the exception of pagination.

ZHOU et al.: TWAM BASED MASTER-SLAVE OPERATION CONTROL 11

[18] Z. Chen, B. Helian, Y. Zhou, and M. Geimer, "An integrated trajectory planning and motion control strategy of a variable rotational speed pump-controlled electro-hydraulic actuator," *IEEE/ASME Trans. Mechatron.*, vol. 28, no. 1, pp. 588–597, Feb. 2023.

[19] J. Mattila, J. Koivumki, D. G. Caldwell, and C. Semini, "A survey on control of hydraulic robotic manipulators with projection to future trends," *IEEE/ASME Trans. Mechatron.*, vol. 22, no. 2, pp. 669–680, Apr. 2017.

[20] J.-P. Humaloja, J. Koivumäki, L. Paunonen, and J. Mattila, "Decentralized observer design for virtual decomposition control," *IEEE Trans. Autom. Control*, vol. 67, no. 5, pp. 2529–2536, May 2022.

[21] J. Shen, J. Zhang, H. Zong, M. Cheng, and B. Xu, "Hierarchical decoupling controller with cylinder separated model of hydraulic manipulators for contact force/motion control," *IEEE/ASME Trans. Mechatron.*, vol. 28, no. 2, pp. 1081–1092, Apr. 2023.

[22] F. Zhang, J. Zhang, M. Cheng, R. Ding, and B. Xu, "Flow manipulability polytope-a novel velocity performance evaluation tool for hydraulic robotic manipulators," *IEEE Trans. Ind. Inform.*, vol. 20, no. 5, pp. 7698–7707, May 2024.

[23] Z. Yao, F. Xu, G.-P. Jiang, and J. Yao, "Data-driven control of hydraulic manipulators by reinforcement learning," *IEEE/ASME Trans. Mechatron.*, vol. 29, no. 4, pp. 2673–2684, Aug. 2024.

[24] W. Deng, H. Zhou, J. Zhou, and J. Yao, "Neural network-based adaptive asymptotic prescribed performance tracking control of hydraulic manipulators," *IEEE Trans. Syst., Man, Cybern.: Syst.*, vol. 53, no. 1, pp. 285–295, Jan. 2023.

[25] W. Sun and Y. Yuan, "Passivity based hierarchical multi-task tracking control for redundant manipulators with uncertainties," *Automatica*, vol. 155, 2023, Art. no. 111159.

[26] Y. Yuan and W. Sun, "An integrated kinematic calibration and dynamic identification method with only static measurements for serial robot," *IEEE/ASME Trans. Mechatron.*, vol. 28, no. 5, pp. 2762–2773, Oct. 2023.

[27] B. Jin, S. Ye, J. Su, and J. Luo, "Unknown payload adaptive control for quadruped locomotion with proprioceptive linear legs," *IEEE/ASME Trans. Mechatron.*, vol. 27, no. 4, pp. 1891–1899, Aug. 2022.

[28] V.-T. Ngo and Y.-C. Liu, "Object transportation with force-sensorless control and event-triggered synchronization for networked uncertain manipulators," *IEEE Trans. Ind. Electron.*, vol. 68, no. 1, pp. 902–912, Jan. 2021.

[29] G. Li, D. Song, S. Xu, L. Sun, and J. Liu, "On perpendicular curve-based model-less control considering incomplete orientation constraint," *IEEE/ASME Trans. Mechatron.*, vol. 26, no. 3, pp. 1479–1489, Jun. 2021.

[30] S. Zhou, C. Shen, Y. Xia, Z. Chen, and S. Zhu, "Adaptive robust control design for underwater multi-dof hydraulic manipulator," *Ocean Eng.*, vol. 248, 2022, Art. no. 110822.

Yangxiu Xia received the B.Eng. degree in ocean engineering and technology in 2022 from Zhejiang University, Hangzhou, China, where he is currently working toward the Ph.D. degree in ocean technology and engineering.

Manzhi Qi received the B.Eng. degree in ocean engineering and technology in 2024 from Zhejiang University, Hangzhou, China, where he is currently working toward the Ph.D. degree in ocean technology and engineering.

Deqing Mei received the B.S. degree from Xidian University, Xi'an, Shaanxi, China, and the Ph.D. degree from Zhejiang University, Hangzhou, Zhejiang, China, in 2000, both in mechanical engineering.

From 2006 to 2008, he was a Visiting Scholar of S.M. Wu Manufacturing Research Center, University of Michigan, Ann Arbor, USA. Currently, he is a Full Professor with the Ocean College, Zhejiang University, Zhoushan, Zhejiang. His research interests include the micro forming and micro-manufacturing, design and micro-manufacturing for hydrogen energy devices, 3-D printing and additive manufacturing, etc.

Shizhao Zhou received the B.Eng. degree in ocean engineering and the Ph.D. degree in ocean technology and engineering from Zhejiang University, Hangzhou, Zhejiang, China, in 2018 and 2024, respectively.

Since 2024, he has been an Associate Professor with the School of Mechanical Engineering and Automation, Fuzhou University, Fuzhou, Fujian, China. His research interests include advanced control of mechatronic hydraulic systems such as hydraulic manipulators.

Zheng Chen (Senior Member, IEEE) received the B.Eng. and Ph.D. degrees in mechatronic control engineering from Zhejiang University, Hangzhou, Zhejiang, China, in 2007 and 2012, respectively.

From 2013 to 2015, he was a Postdoctoral Researcher with the Department of Mechanical Engineering, Dalhousie University, Halifax, NS, Canada. Since 2015, he has been with the Ocean College, Zhejiang University, Zhoushan, Zhejiang, where he was promoted to the rank of Professor in 2020. His research interests mainly focus on the advanced control of robotic and mechatronic system (e.g., nonlinear adaptive robust control, motion control, trajectory planning, tele-robotics, hydraulic system, precision mechatronic system, soft actuator and robot, mobile manipulator, underwater robot, and exoskeleton).